7936 *J. Phys. Chem. A* **2004,** *108,* 7936−7948

Photodissociation Dynamics of Dimethyl Sulfide Following Excitation within the First Absorption Band[†]

Jonathan Barr, Inmaculada Torres, Enrique Verdasco, Luis Bañares, and F. J. Aoiz*

Departamento de Química Física, Facultad de Química, Universidad Complutense de Madrid, 28040 Madrid, Spain

Bruno Martínez-Haya

Departamento de Ciencias Ambientales, Universidad Pablo de Olavide, 41013 Sevilla, Spain

Received: February 13, 2004; In Final Form: April 14, 2004

The technique of resonance-enhanced multiphoton ionization with time-of-flight mass spectrometry (REMPI-TOF MS) has been used to study the photodissociation of fully deuterated dimethyl sulfide (CD_3SCD_3) following excitation at several wavelengths within the first absorption band (215−229 nm). Analysis of measured time-of-flight profiles of the nascent CD_3 products indicates a strongly anisotropic photodissociation, with approximately 70−80% of the available energy appearing as fragment recoil translation. A hybrid statistical−impulsive dissociation model predicts a photolysis wavelength dependence of the translational energy release that compares favorably with experiment, supporting the suggestion (Manaa, M. R.; Yarkony, D. R. *J. Am. Chem. Soc.* **1994**, *116*, 11444) that both the $1^1A''$ and $2^1A''$ excited states play an important role in the photodissociation process. An analysis of nascent CD_3 ($\boldsymbol{\mu}$, **v**, **J**) vector correlations, where the fragments are assumed to recoil axially along the CD_3S-CD_3 bond, adequately accounts for the observed probe laser polarization dependence of velocity-selected REMPI spectra. The weak observed rotational excitation of the methyl fragments originates from zero-point vibrational motion of the dissociating parent molecule.

I. Introduction

Since the pioneering work of Wilson,[1] Bersohn,[2,3] and coworkers, great progress has been made in the study of the photodissociation dynamics of polyatomic molecules. Because more than one excited state must usually be considered upon absorption at ultraviolet wavelengths, the influence of nonadiabatic interactions on product observables has attracted particular attention. An interesting example that has been the subject of recent theoretical[4] and experimental[5−9] work is provided by the photodissociation of CH_3SCH_3 (DMS) in its first absorption band (∼215−230 nm). The electronic configuration of DMS in its ground state can be written as

$$...(1a_2)^2(8a_1)^2(4b_2)^2(3b_1)^2; \qquad \tilde{X}^1A_1$$

where the highest occupied (nonbonding) $3b_1$ molecular orbital is dominated by the $3p_x$ orbital of atomic sulfur, directed perpendicular to the C−S−C plane.[10,11] In C_{2v} symmetry, two low-lying excited electronic states, 1^1B_1 and 1^1A_2, resulting from the promotion of a $3b_1$ electron to a Rydberg-like sulfur 4s orbital ($9a_1$) and to a C−S antibonding valence-like orbital ($6b_2$), respectively, are energetically accessible from the ground, $\tilde{X}^1A_1$ state in the excitation wavelength region of the first absorption band.[12,13] Only the $1^1B_1 \leftarrow \tilde{X}^1A_1$ transition is electric-dipole-allowed in the limit of C_{2v} symmetry, although vibronic coupling of the 1^1B_1 and 1^1A_2 excited states through the CSC asymmetric stretching vibration allows the $1^1A_2 \leftarrow \tilde{X}^1A_1$ transition to steal intensity. Employing the C_s point group, Yarkony et al. calculated potential energy surfaces of the two states, $1^1A''$ and $2^1A''$, and located a seam of conical intersections occurring close to the excited Franck−Condon region accessed from the ground $\tilde{X}^1A_1$ state.[4] The calculations predicted that both the propensity of initial states prepared by absorption and their subsequent dynamics should reflect the strong interaction between the $1^1A''$ and $2^1A''$ states facilitated by the conical intersection. A superposition of vibrational states on both the $1^1B_1(1^1A'')$ and $1^1A_2(2^1A'')$ surfaces is produced following excitation on the first absorption band. The $2^1A''$ state can only dissociate nonadiabatically to the ground-state fragments, a process that can occur efficiently via the surface of conical intersections with the $1^1A''$ state, accessed by stretching of the CS bond and distortions of the CH_3 and CSC bond angles. This readily accessible region of electronic nonadiabaticity has attracted several experimental investigations on the UV photodissociation of DMS. Early studies using flash photolysis[14−16] in the absorption wavelength region 200−300 nm indicated that breakage of the C−S bond via the process

$$CH_3SCH_3 + h\nu \rightarrow CH_3S + CH_3 \qquad (1)$$

is the dominant dissociation pathway. This was later confirmed by Nourbakhsh et al.[17] and Lee et al.[18] at the photolysis wavelength $\lambda_{PHOT} = 193$ nm using translational spectroscopy, which also allowed the direct determination of the CH_3S-CH_3 bond dissociation energy $D_0 \approx 314$ kJ mol^{-1}.

More recently, a number of experimental studies have focused on the dissociation following excitation to the first absorption band using the resonance-enhanced multiphoton ionization time-of-flight (REMPI-TOF) spectroscopy[5,6] and velocity map ion imaging[7,8] techniques. Spectroscopy of the nascent methyl fragments, with the analysis of time-of-flight (TOF) profiles

---

[†] Part of the special issue “Richard Bersohn Memorial Issue”.

* Corresponding author. E-mail: aoiz@quim.ucm.es.

10.1021/jp049344s CCC: $27.50

and ion images, indicated that approximately 80% of the total available energy is deposited into fragment translation, approximately 5% is disposed into internal CH_3 modes, and the remaining 15% appears as internal excitation of the SCH_3 fragment.[5-8] In addition, the spatial anisotropy parameter β was found to be close to the limiting value expected for a perpendicular-type transition ($\beta = -1$). These findings allowed the salient features of the dissociation process to be surmised, suggesting a prompt dissociation mechanism that induces effective energy transfer into fragment translation.[5-8]

Although the energy partitioning and anisotropy provide a coarse-grained picture, understanding of the photodissociation mechanism can be greatly enhanced by specifying the correlation between the vectors **J**, the angular momentum, and **v**, the recoil velocity of the fragments, in a molecular frame defined by $\boldsymbol{\mu}$, the transition dipole moment of the parent molecule at the time of excitation. To this end, a recent study[9] of DMS in the first absorption band (at 219 nm) sought to characterize the laboratory-frame (**v**, **J**) alignment of the methyl photofragments immediately after dissociation. Invoking an impulsive dissociation model, where the fragments recoil axially along the CH_3S-CH_3 bond, core-sampled[19] REMPI spectra of the nascent fragments were adequately simulated. The success of the simple dissociation model allowed the nascent rotational populations and molecular-frame alignment (i.e., K-state propensity, where K is the quantum number of the projection of **J** onto the symmetric top axis) of the methyl fragment to be deconvoluted from laboratory-frame alignment effects, an important procedure if the latter are strong.

In light of this new insight into the dissociation mechanism, the present work describes measurements, using the REMPI-TOF technique, over a range of photolysis wavelengths ($\lambda_{\text{PHOT}} = 215-230$ nm) corresponding to diffuse vibrational features on the first absorption band, exploring three key aspects. First, the photofragment recoil energy distributions and β parameters are obtained from the TOF profiles using an accurate instrumental response function, revealing quite a striking correlation between energy disposal/anisotropy and photolysis wavelength. Second, the aforementioned characterization of the (**v**, **J**) alignment of the methyl photofragments, where cylindrical symmetry of the **J** vector about **v** is presumed, is extended to include possible coherence in a frame attached to $\boldsymbol{\mu}$. Finally, the nascent methyl rotational distributions and molecular-frame alignment (K-state propensity) obtained from REMPI spectra, deconvoluted from laboratory-frame-alignment effects, are examined in closer detail, indicating a correlation with the internal motion of the dissociating parent in accordance with an axial, impulsive-type dissociation. These findings, together with the results of previous experimental and theoretical work, are used to discuss further the qualitative features of the excited-state surface, upon which the dynamics of the photodissociation intimately depend.

II. Experimental Procedures

The REMPI-TOF apparatus has been described in detail previously.[6,20] Briefly, approximately 200 Torr of pure CD_3-SCD_3 (hereafter, DMS-d_6) vapor was expanded through a pulsed valve (nozzle orifice diameter ≈ 0.05 cm, opening time ≈ 300 μs) into an evacuated chamber (typical working pressure ≈ 10^{-6} mbar), forming a free jet that is perpendicularly intersected ∼5 cm downstream by two counterpropagating laser beams.

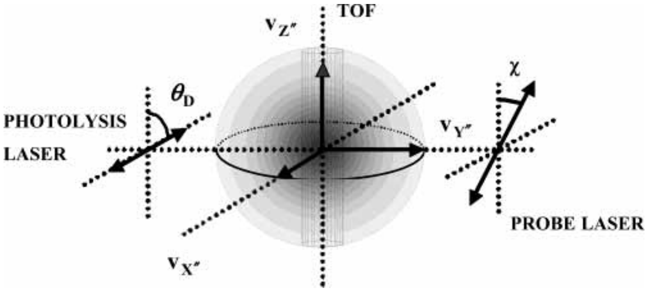

Figure 1. Schematic representation of the experimental geometry showing the counterpropagating photolysis and probe laser beams directed perpendicularly to the TOF axis. The angles θ_D and χ are between the TOF axis and the electric field vectors of the photolysis and probe lasers, respectively. The vertical cylinder depicts the core sampling of ions with reduced velocity projection $v_{Z''}/v \approx 1$ facilitated by operation of the TOF mass spectrometer with a low ion extraction field, rejecting off-axis-traveling CD_3 fragments.

The photolysis laser, the frequency-mixed output of a Nd:YAG-pumped dye system, is fired at an optimal time (∼400 μs) after the pulsed valve, interacting with the early edge of the free jet such that cluster formation is minimized. Around 10 ns later, the tunable frequency-doubled output of a separate Nd:YAG-pumped dye laser (285−287 nm) delivers the probe radiation. Two double Fresnel−Rhomb prisms controlled the polarization direction of the photolysis and probe radiation independently. The CD_3 photofragments were selectively ionized by (2 + 1) REMPI via the $(4p_z)\,^2A_2'' \leftarrow \tilde{X}\,^2A_2''$ transition.[21] Ions are extracted from the interaction region using continuous voltages applied to a series of stainless steel plates (6 × 6 × 0.1 cm) that each house a 2-cm-diameter aperture and are arranged in a Wiley−McLaren[22]-type setup. The extraction region consists of two plates, the repeller (P1) (furthest from the detector), and the extractor (P2), mutually separated by 1 cm and thus creating the extraction field, E_{ex}, which can be adjusted between 0 and 2000 V cm^{-1}. A third plate (P3), an additional 1 cm closer to the detector, is held at ground potential and defines the Wiley−Mclaren acceleration region.[22] The ions pass an additional 12 cm upstream before encountering the final collimating plate (P4), also of 2-cm aperture diameter, which is held at ground potential. After traversing a second field-free region (∼16-cm flight path) the ions are detected by a microchannel plate detector. The resulting ion signal is amplified and passed to a computer-interfaced digital oscilloscope for data analysis.

The REMPI-TOF method is sensitive to the projection of the 3D velocity distribution of photofragments onto the TOF detector axis. To extract meaningful information, this transformation must be accurately simulated, taking into account any inherent velocity discrimination effects of the system. Taking Z'' as the TOF detector axis, then, for a trajectory with an off-axis component of velocity $v_{Y''}$ (or $v_{X''}$), it can be shown that an ion formed at the center of the extraction region will reach the detector only if

$$v_{Y''}t < R \qquad (2)$$

where t is the time of flight to P4 and R is the radius of the aperture in P4. Thus, for sufficiently high recoil energies, small extraction voltages (longer times, t) discriminate against laterally traveling photofragments.

The capability of the REMPI-TOF system to discriminate against photofragments recoiling laterally to the TOF axis with $v_{Y''}t > R$ can be employed to generate an arrival distribution of photofragments that is a one-dimensional sample through the core of the complete velocity sphere, as depicted schematically in Figure 1. In the extreme case of this “core-sampling”[19,23] detection scheme, only fragments recoiling up or down, parallel

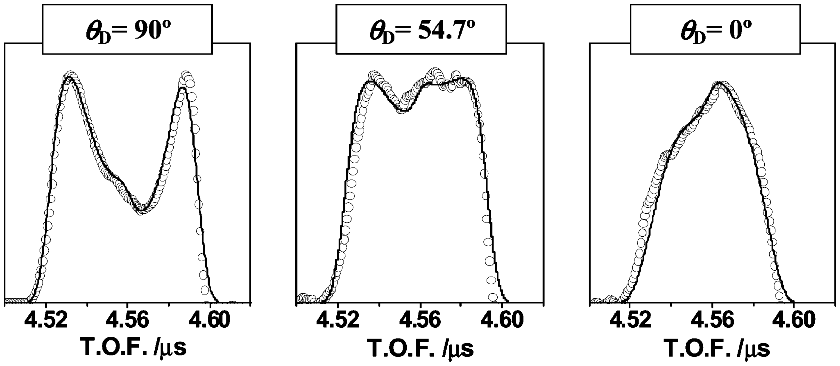

Figure 2. REMPI-TOF profiles (open circles) of the CD_3 fragments following photodissociation of DMS-d_6 at $\lambda_{PHOT} = 215$ nm measured on the maximum of the Q branch of the $(4p_z)^2A_2'' \leftarrow X^2A_2''\,0_0^0$ transition for three different angles, θ_D, between the photolysis laser electric vector, $\hat{\epsilon}_D$, and the TOF detector axis, Z''. The solid curves represent calculated simulations of the profiles (see text).

to the extraction direction, i.e., with reduced velocity projection along the TOF axis $v_{Z''}/v \approx 1$, are detected. As has been shown in previous work,[9] this apparent disadvantage of the detection system is particularly useful for the characterization of ($\boldsymbol{\mu}$, **v**, **J**) correlations.

In the present work, photofragment recoil energy and dissociation anisotropy information, where nascent rotational state selection is not necessary, was extracted from TOF profiles measured on the maximum of the Q branch of the two-photon $(4p_z)^2A_2'' \leftarrow \tilde{X}^2A_2''\,0_0^0$ transition. No core sampling was employed in those experiments, with the ion extraction field chosen to satisfy eq 2 (typically, $E_{ex} \approx 240$ V cm^{-1}) for the majority of the photofragment velocity distribution produced by the dissociation.

For experiments that do require rotational-state specificity of the photofragments, as is the case in the REMPI spectroscopic determination of nascent rotational-state distributions, the much weaker O, P, R, and S transitions must be probed. The advantage of a core-sampling detection scheme is then two-fold. First, velocity selection dramatically increases the sensitivity of the experiment to the ($\boldsymbol{\mu}$, **v**, **J**) correlations created by the photodissociation process. Second, the low extraction field (typically, $E_{ex} \approx 80$ V cm^{-1}) allows the separation of the relatively weak REMPI signal on the O, P, R, and S transitions from the nonresonant contamination (insignificant on the Q branch) of slow, isotropic CD_3^+ ions formed by multiphoton dissociative ionization of the parent molecule (adiabatic ionization potential = 8.71 eV),[7,8,11] allowing clean REMPI spectra to be obtained.

III. Results and Analysis

A. REMPI-TOF Profiles: Anisotropy and Recoil Energy Distributions. The REMPI-TOF profiles, $I(t;\theta_D)$, of the CD_3 fragments measured following the photodissociation of DMS-d_6 at $\lambda_{PHOT} = 215$ nm for different angles θ_D between the TOF axis and the photolysis laser electric field vector $\hat{\epsilon}_D$ are shown in Figure 2. The profiles were obtained at the probe laser wavelength corresponding to the maximum observed intensity on the congested Q branch of the methyl photofragment $4p_z 0_0^0$ transition. In accordance with previous studies,[5] the CD_3^+ ion signal showed a roughly linear dependence on the photolysis laser photon flux, indicating that the methyl fragments are produced at the one-photon excitation level. The slight asymmetric appearance of the profiles is a consequence of the less efficient detection of ions flying away from the detector (longer times t in eq 2), although it is evident from the excellent agreement between the experimental and simulated profiles that this effect is well modeled by the instrumental response function (see below). The contrasting appearances of the profiles at different polarizations of the photolysis laser, θ_D, imply that the photodissociation occurs with a significantly negative recoil anisotropy parameter, β, in agreement with previous investigations[6] at $\lambda_{PHOT} = 229$ nm.

The use of the REMPI-TOF technique as a means of measuring kinetic energy release and anisotropy in molecular photodissociation has been described by several authors.[24−27] For a single-photon dissociation process induced by linearly polarized light in an isotropically oriented sample, the angular distribution of photofragments, $I(\theta)$, is axially symmetric with respect to the electric field vector, $\hat{\epsilon}_D$, of the light and can be expressed as[28]

$$I(\theta) = \frac{1}{4\pi}[1 + \beta P_2(\cos\theta)] \qquad (3)$$

where θ is the fragment ejection angle relative to $\hat{\epsilon}_D$, β is the recoil anisotropy parameter, and P_2 is the second Legendre polynomial. The REMPI-TOF technique measures the projection of the 3D recoil distribution along the TOF-MS axis. Transforming the angular distribution in eq 3 to the laboratory coordinate system in which the Z'' axis is the TOF-MS axis and summing over the recoil speed distribution, $g(v)$, gives the projected distribution[29]

$$f(v_{z''},\theta_D) = \int_{|v_{z''}|}^{v_{\max}} \frac{g(v)}{2v}\left[1 + \beta(v)P_2(\cos\theta_D)P_2\left(\frac{v_{z''}}{v}\right)\right] \mathrm{d}v \qquad (4)$$

where $v_{Z''}$ is the velocity component along the Z'' axis, v is the speed of the fragments, and θ_D is the angle between the Z'' axis and the photolysis electric field vector $\hat{\epsilon}_D$. Other terms in eq 4 caused by (**v**, **J**) correlations,[24] which are the focus of section III.B, were disregarded for the purpose of extracting speed distributions and anisotropy parameters from the profiles, the shape of which are, in any case, dominated by the ($\boldsymbol{\mu}$, **v**) correlation. The inclusion of these extra terms does not change the extracted anisotropy parameters and speed distributions within experimental uncertainty. Under space-focusing conditions,[22] the experimental TOF spectra, $I(t;\theta_D)$, can be transformed to the velocity domain, $I(v_{Z''},\theta_D)$, by the relation

$$v_{z''} = \frac{qE_{ex}(t - t_0)}{m} \qquad (5)$$

where q and m are, respectively, the charge and mass of the photofragment and t_0 is the mean time of flight of the ion. To simulate the velocity-domain, $I(v_{Z''},\theta_D)$, profile and extract the dynamically significant terms $g(v)$ and $\beta(v)$, the expression for $f(v_{Z''},\theta_D)$ (eq 4) must be convoluted with an appropriate

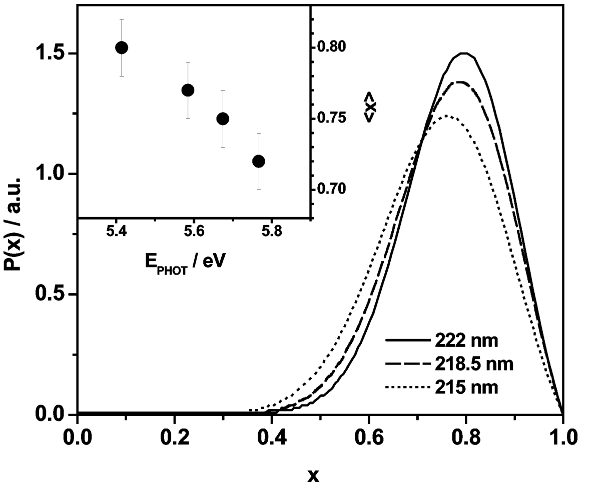

Figure 3. Recoil energy distributions, $P(x)$, obtained from the forward analysis (see text for details) of methyl fragment REMPI-TOF profiles obtained at the different photolysis wavelengths studied in the first absorption band ($\lambda_{\mathrm{PHOT}} = 215$, 218.5, 222, and 229 nm). The inset plot shows the photolysis energy, E_{PHOT}, dependence of the average recoil energy, $\langle x \rangle$, correlating with ground-vibrational-state methyl products.

instrumental response function, including the duration of the laser pulse, small deviations from the space-focusing conditions, contamination by the nonresonant $CD_3{}^+$ signal described earlier, and any velocity-discriminating effect of the TOF detector (see section II). The latter was calculated with the aid of ion trajectory simulations using the SIMION 5.0 computer program.[30]

At the "magic angle" of $\theta_D = 54.7°$, $f(v_{Z''},\theta_D)$ is independent of β, allowing the speed distribution $g(v)$ to be obtained directly by differentiation of eq 4

$$g(v) = -2v \frac{d}{dv_{Z''}} f(v,54.7°)\bigg|_{v_{Z''}=v} \tag{6}$$

This direct inversion procedure requires accurate knowledge of the instrumental function, as well as the use of numerical filters to suppress the effects of high-frequency noise. Alternatively, the forward convolution method of Bergmann and coworkers[26] can be used. Application of eq 6 to the magic-angle TOF profile, $I(v_{Z''},54.7°)$, provides an estimate of the speed distribution $g(v)$, which is then used to determine the form of a representative velocity distribution obtained via the transformation $g(v) = P(E_{\mathrm{rec}})|dE_{\mathrm{rec}}/dv|$ from a modified Gaussian recoil energy distribution function[6]

$$P(x) = Nx(1 - x) \exp\left[-\left(\frac{x - x_0}{\Delta x}\right)^2\right] \tag{7}$$

where $x = E_{\mathrm{rec}}/E_{\mathrm{max}}$ is the fraction of the total available energy, E_{max}, appearing as fragment translational recoil energy; x_0 and Δx are fit parameters; and N is a normalization constant. Convolution of $P(x)$ with the instrument response function yields simulated TOF profiles that can be compared with experimental results. Having obtained the speed distribution $g(v)$, the β parameter can be determined by iterative simulation of the measurements at $\theta_D = 0°$ and 90°, with the fits at the three different geometries providing confidence for the predetermined $g(v)$.

As can be seen in Figure 2, excellent agreement between the measured and simulated profiles is found using the function $P(x)$ with a single velocity-independent anisotropy parameter β. Figure 3 shows the translational energy distributions obtained using the forward-analysis procedure at each photolysis wavelength studied. The distributions indicate that a high fraction of available energy is deposited into fragment translational recoil, $\langle x \rangle \approx 0.7-0.8$ (see inset of Figure 3), decreasing progressively as a function of excitation energy. Identical best-fit anisotropy parameters, $\beta = -0.8 \pm 0.1$, were determined at the three different photolysis wavelengths, in agreement with the near limiting value determined in previous work[6] at $\lambda_{\mathrm{PHOT}} = 229$ nm.

B. Internal Energy and Alignment of the CD_3 Fragment. Previous investigations of the photodissociation of DMS-h_6 in the first absorption band[5] reported only the weak presence of hot bands in the REMPI spectrum, thus establishing that the methyl photofragment is vibrationally cold. The rotational distribution is probed through the $4p_z 0_0^0$ transition of the nascent methyl fragments. Figure 4a shows the high-frequency part (Q, R, and S branches) of the (2 + 1) REMPI spectrum of this transition after the photodissociation of DMS-d_6 ($\lambda_{\mathrm{PHOT}} = 218.5$ nm) at three different angles, $\chi = 0°$, 35°, and 90°, between the probe laser electric vector, $\hat{\epsilon}_P$, and the TOF detection axis, Z''. The O and P branches were not included in the analysis because of contamination of those transitions by the 1_1^1 hot band.[6]

The marked dependence of the REMPI spectra on the polarization of the probe laser indicates that the methyl photofragments are strongly aligned in the laboratory frame. This can be understood when one considers that, for the present case of a high-recoil-energy-release photodissociation employing a low extraction field, the extreme case of the core-sampling detection scheme (see section II) is reached. Under these circumstances, discrimination against ions with even a slight component of off-axis velocity will occur. The result is a highly anisotropic effective spatial distribution of the **J** vector, rather than the weaker, translationally averaged anisotropy that is observed if the entire velocity "sphere" is collected. Evidently, the effects of these ($\boldsymbol{\mu}$, **v**, **J**) correlations must be deconvoluted in the analysis of the REMPI spectra for accurate nascent rotational state populations to be extracted. The essential features of this procedure are explained in the following paragraphs.

Most previous work concerning the measurement of photofragment ($\boldsymbol{\mu}$, **v**, **J**) vector correlations has involved the measurement of Doppler-resolved laser-induced fluorescence (LIF) line shapes,[31] REMPI/TOF profiles,[24] or ion images[32−34] as a function of experimental geometry and type of probe transition. The interpretation of the LIF and REMPI work is generally based on the theoretical treatment of Dixon[35] in which the mutual arrangement of both angular momentum and velocity are described by a correlated (**v**, **J**) angular distribution $P(\omega_t', \omega_r')$, where $\omega_t'(\theta_t',\phi_t')$ and $\omega_r'(\theta_r',\phi_r')$ are the angular coordinates of **v** and **J** defined in the molecular frame that has its z' axis parallel to the parent transition dipole moment $\boldsymbol{\mu}$ (see lower panel in Figure 5). This distribution is expressed as an expansion on the basis of the bipolar harmonics $B_{KQ}(k_1,k_2,\omega_t',\omega_r')$, whose coefficients $b_Q^K(k_1,k_2)$ are the bipolar moments, which completely characterize the angular relation between the vectors $\boldsymbol{\mu}$, **v**, and **J**.

To relate the body-fixed frame (x', y', z') bipolar moments $b_Q^K(k_1,k_2)$ to experimental observables, the system geometry must be fully specified. The various frames of reference that are necessary in this work are defined in Figure 5. The dissociation frame (X, Y, Z) is defined with the Y axis as the direction of propagation of the dissociation laser and the Z axis as the direction of its electric field vector, i.e., $Z \parallel \hat{\epsilon}_D$. The other two important laboratory frames are defined in terms of Euler rotations with respect to this frame. The TOF detector frame

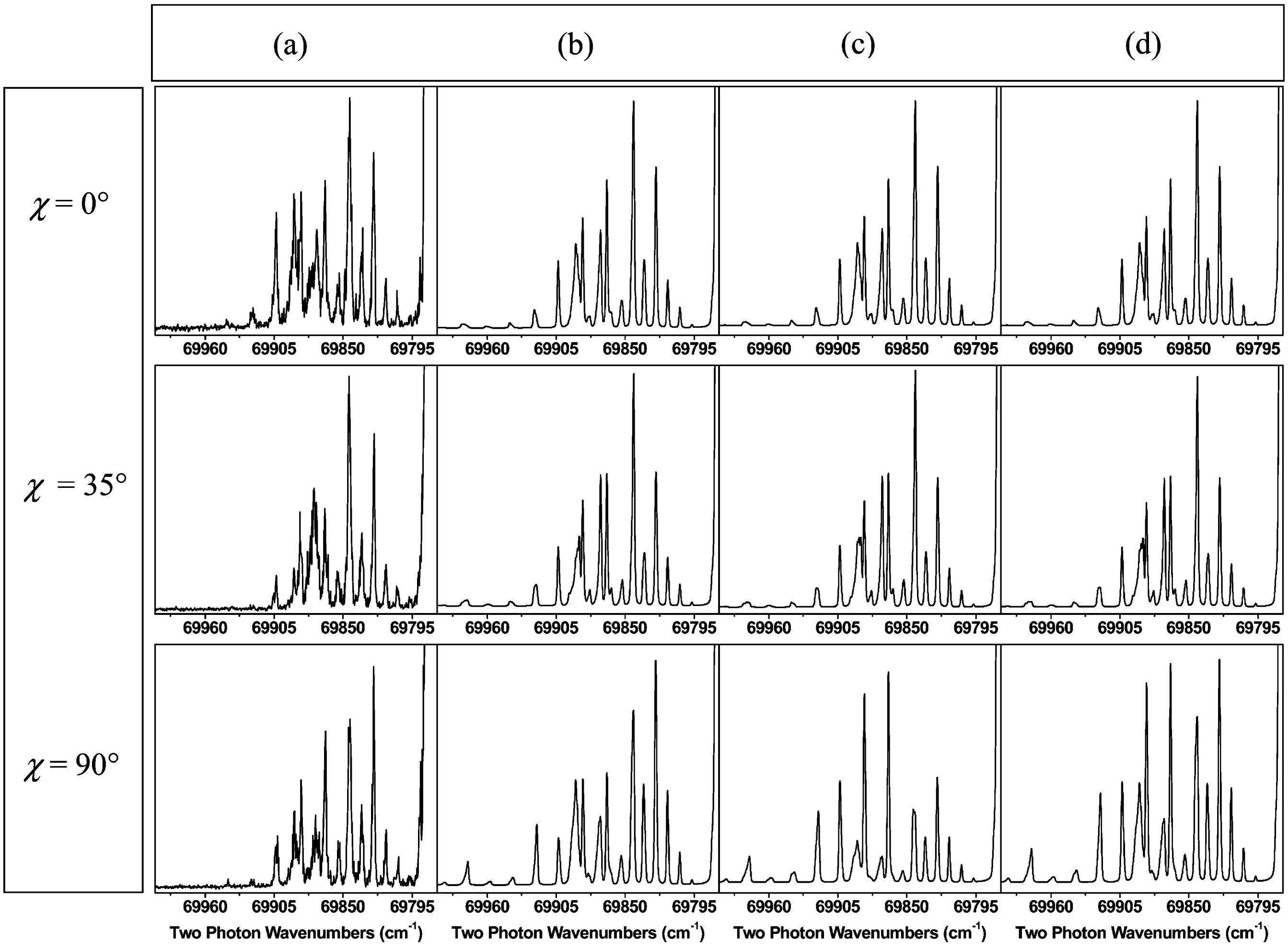

Figure 4. (a) Experimental (2 + 1) REMPI spectra of the CD_3 $(4p_z)^2$ $A_2'' \leftarrow X^2A_2'' 0_0^0$ transition for three different angles, $\chi = 0°$, 35°, and 90°, between the probe laser electric vector, $\hat{\epsilon}_P$, and the TOF detector axis, Z''. The simulated spectra are shown in b−d. In d, **J** is cylindrically symmetric about the **v** vector; in b and c, the **J** vector lies in the $x'z'$ and $x'y'$ planes, respectively (see text).

(X'', Y'', Z'') is obtained by an Euler rotation (0, θ_D, 0) from the dissociation frame and has its Z'' axis defined as the TOF-MS axis. The probe frame (X''', Y''', Z''') is defined with the Y''' axis as the propagation direction of the probe light and Z''' as the direction of its electric field vector, $Z''' \parallel \hat{\epsilon}_P$, and is obtained by the rotation (0, θ_P, 0) from the dissociation frame, θ_P being the angle between $\hat{\epsilon}_P$ and $\hat{\epsilon}_D$.

Dixon[35] and Cline et al.[36] have described the transformation of the body-fixed $P(\omega_t', \omega_r')$ to the velocity-dependent angular momentum polarization moments[37] in the dissociation frame (X, Y, Z), $A_q^{R(k)}$, for single-photon electric dipole excitation of the parent molecule, thus allowing the bipolar moments to be related to the intensity of a probing transition for a given velocity projection along the detector axis. Several authors[24,36,38] have described fitting procedures for experimental TOF profiles where the geometry and polarization of the dissociating and probe radiation are controlled, allowing for the determination of the various bipolar moments related to the ($\boldsymbol{\mu}$, **v**, **J**) vector correlation.

In the present work, the nonresonant ion signal mentioned in section II prevents the measurement of clean TOF profiles on all probe transitions of the methyl photofragment except the spectrally congested Q branch. Instead, a forward-analysis-type approach is applied with a presumed ($\boldsymbol{\mu}$, **v**, **J**) correlation, based on a dissociation mechanism suggested by previous studies that is used to calculate the expectation values of the bipolar moments from the semiclassical arguments listed in Table 2 of ref 35. Model $A_q^{R(k)}$ moments can then be calculated and used to simulate the REMPI spectra at the different experimental geometries. Comparison of the calculated polarization-dependent REMPI spectra with experiment serves as an evaluation of the model ($\boldsymbol{\mu}$, **v**, **J**) correlation.

A model photodissociation is proposed in which a pure perpendicular-type absorption is immediately followed by an impulse passing axially along the breaking CS−C bond, directly through the center of mass of the methyl fragment. This is reasonable because previous investigations have indicated a strongly anisotropic photodissociation, where most of the available energy is channeled into translational motion of the fragments, imparting only weak internal excitation of the methyl fragment. Within this model, only parent vibrational and rotational motion can transfer angular momentum to the methyl fragment, although under the free-jet-cooled conditions of the current work, only low-J states are excited, the rotation of which will be mostly converted into orbital angular momentum of the half-collision. For this reason, only the effect of parent vibrational motion (mostly zero-point) on the methyl fragment rotational distribution and alignment is considered here.

Of the 21 fundamental vibrations of DMS discussed by Allkins and Hendra,[39] the two torsional (ν_1 and ν_2) and four CD_3 rocking (ν_6−ν_9) modes are most strongly correlated with methyl fragment rotational excitation. Most of the torsional energy will be transferred to spinning rotational motion of the fragments, as no corresponding vibrational modes exist in either

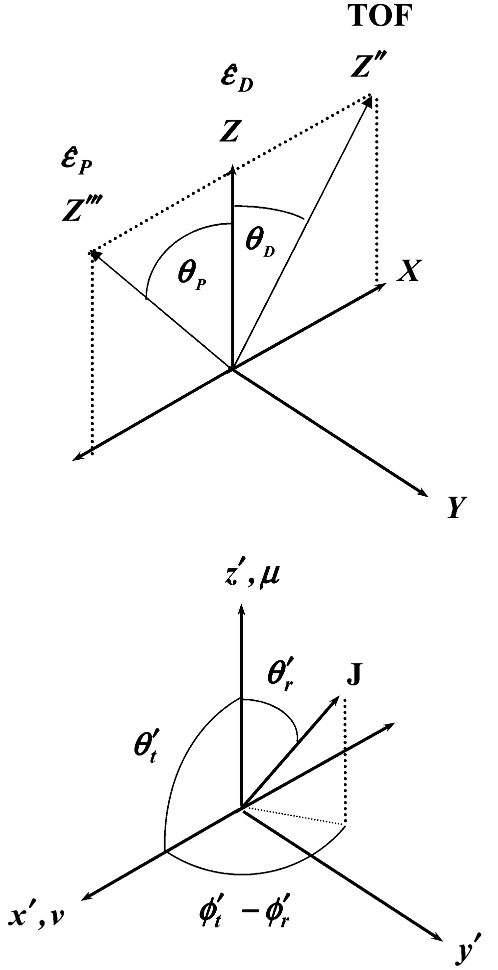

Figure 5. Frames of reference used in the analysis. Upper panel: The dissociation frame (X, Y, Z) is defined with the Y axis as the direction of propagation of the dissociation laser and the Z axis as the direction of its electric field vector, $Z \parallel \hat{\epsilon}_D$. The TOF detector ($R''$) and probe ($R'''$) frames are obtained by respective (0, θ_D, 0) and (0, θ_P, 0) Euler rotations from the dissociation frame. Lower panel: The body-fixed system used to calculate the model bipolar moments, with the z' axis parallel to the parent transition dipole moment $\boldsymbol{\mu}$ at the instant that the photolysis radiation is absorbed.

CD_3 or SCD_3. In the case of the rocking-type vibrational modes, it is difficult to assess quantitatively the expected energy transfer without the aid of detailed dynamical calculations, although it is clear that this type of motion will give rise to tumbling methyl fragments. Tacitly assuming that the C_3 axis of the methyl fragment is parallel to the recoil velocity vector, the torsional vibrational modes will give rise to high-K'' state propensity ($\mathbf{v} \parallel \mathbf{J}$ alignment), whereas low-K'' state propensity ($\mathbf{v} \perp \mathbf{J}$ alignment) would be expected from the contribution of the rocking modes.

The angle θ'_t, between the parent molecule transition moment $\boldsymbol{\mu}$ and the translational velocity vector $\mathbf{v}$ of the CD_3 fragment, is fixed to 90° for this purely perpendicular-type transition. Within the model, the angle θ'_{tr} (ω'_{tr} in the notation of ref 38) between $\mathbf{J}$ and $\mathbf{v}$ and the angle θ'_r can be estimated by invoking the vector model of the angular momentum $\mathbf{J}$.[37] The state $|JK\rangle$ of the CD_3 fragment is then represented by a vector of length $\sqrt{J(J+1)}$ making a fixed projection K on the methyl C_3 axis that is also coincident with the velocity vector $\mathbf{v}$. The average angle $\langle\theta'_{tr}\rangle$ is then given by

$$\langle\theta'_{tr}\rangle = \cos^{-1}\left\{\frac{K}{[J(J+1)]^{1/2}}\right\} \qquad (8)$$

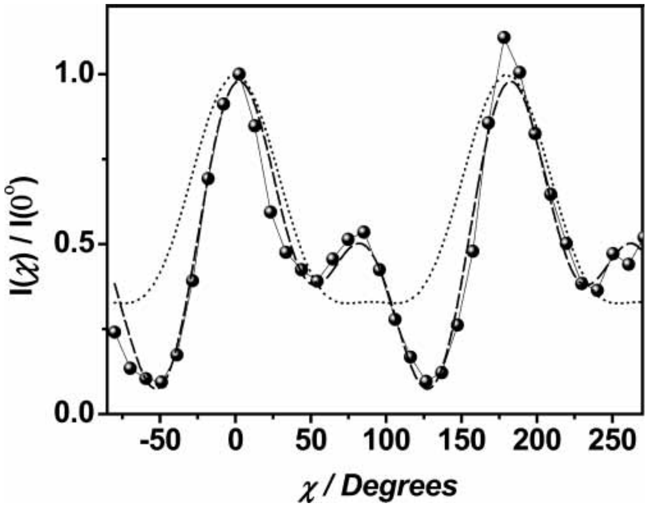

Figure 6. (2 + 1) REMPI ion signal (spheres) of the nascent CD_3 $(4p_z)^2A''_2 \leftarrow X^2A''_2 0^0_0$ R(5) transition versus the angle χ between the electric field vector of the probe laser, $\hat{\epsilon}_P$, and the TOF axis, Z''. The dotted line shows a constrained least-squares fit of eq 9 to the data with ${}^{R''}A^{(k)}_{q\neq 0} = 0$. The dashed line represents a least-squares fit of eq 12 to the data.

In previous work,[9] the distribution of $\mathbf{J}$ was assumed to be cylindrically symmetric with respect to the recoil velocity vector $\mathbf{v}$. Here, the two extreme cases of deviation from this assumption are also considered: (i) The $\mathbf{J}$ vector is confined to the plane $x'z'$; thus, $\phi'_r - \phi'_t = 0$, and the angle θ'_r between $\mathbf{J}$ and $\boldsymbol{\mu}$ is $\theta'_r = \pi/2 - \theta'_{tr}$. (ii) $\mathbf{J}$ is restricted to lie in the plane $x'y'$; thus, $\theta'_r = \pi/2$, and $\langle\theta'_{tr}\rangle = \phi'_r - \omega'_t$. In both cases, high K values converge to $\mathbf{J}$, $\mathbf{v} \perp \boldsymbol{\mu}$ at increasing values of $\mathbf{J}$.

The two-photon intensity I of the nascent CD_3 fragment $4p_z$ 0^0_0 transition can be written as[40]

$$I = Cn(N'',K'')\sum_{k,q} P^k_q(N'',K'';N',K';\Omega)\ {}^{R}A^{(k)}_q(N'',K'') \qquad (9)$$

where C is a detection constant; n is the total population of the nascent state (N'', K''); and the P^k_q are two-photon line-strength factors, the calculation of which is described elsewhere.[40] (Note that N denotes the total angular momentum excluding the spin of the unpaired electron; fine-structure depolarization effects are taken into account through the line-strength factors.[40]) For consistency with earlier work[9] the alignment parameters ${}^{R''}A^{(k)}_q$ are defined in the detection laboratory frame with respect to the TOF-MS axis Z''. These are obtained from the ${}^{R}A^{(k)}_q$ moments in the dissociation laboratory frame by the transformation

$${}^{R''}A^{(k)}_q = \sum_{q'=-k}^{k} D^k_{q'q}(0,\theta_D,0)\ {}^{R}A^{(k)}_{q'} \qquad (10)$$

Note that, for the present case, where $v_{Z''}/v \approx 1$, the ${}^{R''}A^{(k)}_q$ are equivalent to the molecular-frame polarization parameters $a^{(k)}_q(\perp)$ of Rakitzis et al. for which explicit expressions in terms of the bipolar moments are given in ref 41.

B.1. Polarization Scans: Determination of the Apparent ${}^{R''}A^{(k)}_{q'}$(app) Moments. Figure 6 plots the intensity of the R(5) transition as a function of χ, the angle between the electric field vector of the probe laser, $\hat{\epsilon}_P$, and the TOF axis Z''. In accordance with eq 9, a linear combination of the individual unresolved K''-state alignment moments weighted by the population $n(N'',K'')$, and appropriate $P^k_q(N_i,K_i;N_f,K_f;\Omega)$ line-strength factors determine the intensity change that is observed. In previous work,[9] a constrained least-squares fit to the data in Figure 6

TABLE 1: Experimentally Determined Apparent Moments ${}^{R''}A_{q'}^{(k')}$(app)/${}^{R''}A_0^{(0)}$(app) for the R(5) Transition of the Nascent Methyl Fragments

${}^{R''}A_{q'}^{(k')}$(app)/${}^{R''}A_0^{(0)}$(app)	experimental value
$k = 2, q = 0$	0.7 ± 0.1
$k = 4, q = 0$	-1.3 ± 0.1
$k = 2, q = 1$	-0.6 ± 0.1
$k = 4, q = 1$	-0.06 ± 0.04

with ${}^{R''}A_{q\neq 0}^{(k)} = 0$ was only partly satisfactory. Although the maximum observed when the probe electric field vector was parallel to the TOF detection axis was qualitatively reproduced, the asymmetric intermediate maximum was barely present in the simulations. The reason for this discrepancy was postulated as the contribution of ${}^{R''}A_q^{(k)}$ moments with $q \neq 0$, which are zero within the assumption that the **J** vector is cylindrically symmetric about **v**. When the probe laser propagation direction is fixed, the noncylindrically symmetric moments have line strengths P_q^k that are linearly dependent on those for the cylindrically symmetric moments, thus impeding the unique determination of the real moments. Kummel et al.[40,42,43] expressed the P_q^k of eq 9 in terms of a set of mutually independent $P_{q'}^{k'}$(ind) over the plane of space in which the probe laser electric field vector rotates

$$P_q^k(N_i,K_i,N_f,K_f,\Omega) = \sum_{k',q'} c(k,q,k',q',N_i,K_i,N_f,K_f) \times P_{q'}^{k'}(N_i,K_i,N_f,K_f,\Omega)(\text{ind}) \tag{11}$$

where the expansion coefficients are specific to a given rotational transition and can be derived either numerically, by least-squares fitting of eq 11, or analytically,[42] by multiplying both sides of eq 11 by $P_{q'}^{k'}$(ind) and integrating over the plane of rotation of the probe electric field vector. Substituting eq 11 into eq 9, grouping together all coefficients for each $P_{q'}^{k'}$(ind) factor, and renaming these coefficients as the apparent moments ${}^{R''}A_{q'}^{(k')}$(app) gives an expression for the total intensity in terms of mutually independent line strengths

$$I = Cn(N'',K'')\sum_{k',q'} P_{q'}^{k'}(N'',K'';N',K';\Omega)(\text{ind})\ {}^{R''}A_{q'}^{(k')}(N'',K'',N',K')(\text{app}) \tag{12}$$

where

$${}^{R''}A_{q'}^{(k')}(\text{app}) = \sum_{k,q} c(k,q,k',q') A_q^{(k)} \tag{13}$$

In eq 13, k' and q' are restricted to the ranks and components of the independent moments of the line strength, $P_{q'}^{k'}$(ind), but k and q are completely general. Although the current experimental configuration cannot provide a measurement of the real alignment moments, its sensitivity to the apparent moments is useful for comparison with theoretical values derived from the model dissociation process. Least-squares fitting of the data shown in Figure 6 to eq 12 yields the ${}^{R''}A_{q'}^{(k')}$(app)/${}^{R''}A_0^{(0)}$(app) moments listed in Table 1. Also shown in the figure is a comparison with the constrained fit from previous work,[9] using eq 9, where ${}^{R''}A_q^{(k)}$ moments with $q \neq 0$ were assumed to be zero. Evidently, the apparent moments provide a much more satisfactory fit to the experimental data.

Calculated ${}^{R''}A_{q'}^{(k')}$(app)/${}^{R''}A_0^{(0)}$(app) moments within the impulsive model dissociation, using Table 2 of ref 35 and eqs 8−13, are reported in Tables 2 and 3 for the two limiting cases where **J** is confined to the $x'z'$ and $x'y'$ planes, respectively.

TABLE 2: Model ${}^{R''}A_{q'}^{(k')}$(app)/${}^{R''}A_0^{(0)}$(app) Parameters for the $N'' = 5$ State of the Nascent Methyl Fragments, where J is Confined to the Plane $x'z'$[a]

K''	${}^{R''}A_0^{(2)}$	${}^{R''}A_2^{(2)}$	${}^{R''}A_0^{(4)}$	${}^{R''}A_2^{(4)}$	${}^{R''}A_0^{(2)}$(app)	${}^{R''}A_0^{(4)}$(app)
0	−1	0.612	0.375	−0.198	−0.872	0.471
1	−0.9	0.592	0.255	−0.146	−0.865	0.336
2	−0.6	0.531	−0.048	−0.011	−0.810	−0.027
3	−0.1	0.429	−0.361	0.154	−0.612	−0.474
4	0.6	0.286	−0.395	0.257	−0.072	−0.664
5	1.5	0.102	0.254	0.17	1.107	0.039

[a] See text for details.

TABLE 3: Model ${}^{R''}A_{q'}^{(k')}$(app)/${}^{R''}A_0^{(0)}$ Parameters for the $N'' = 5$ State of the Nascent Methyl Fragments, where J is Confined to the Plane $x'y'$[a]

K''	${}^{R''}A_0^{(2)}$	${}^{R''}A_2^{(2)}$	${}^{R''}A_0^{(4)}$	${}^{R''}A_2^{(4)}$	${}^{R''}A_0^{(2)}$(app)	${}^{R''}A_0^{(4)}$(app)
0	−1	−0.612	0.375	0.213	−1.30	0.08
1	−0.9	−0.592	0.255	0.158	−1.00	0.03
2	−0.6	−0.531	−0.048	0.013	−0.25	−0.09
3	−0.1	−0.429	−0.361	−0.163	0.64	−0.14
4	0.6	−0.286	−0.395	−0.268	1.41	0.01
5	1.5	−0.102	0.254	−0.161	1.89	0.51

[a] See text for details.

For linearly polarized photolysis and probe radiation, within the approximation of a perfect core-sampling experiment ($v_z/v = 1$) with a pure, single-photon, perpendicular transition ($\beta = -1$), ${}^{R''}A_{q'}^{(k')}$ moments with odd q or even $q > 2$ are zero. Deviations from the model give rise to the experimental nonzero ${}^{R''}A_1^{(2)}$(app) and ${}^{R''}A_1^{(4)}$(app) moments (see Table 1); only the ${}^{R''}A_0^{(k')}$(app) parameters can be compared with the values obtained from the model impulsive dissociation. The experimentally obtained ${}^{R''}A_0^{(2)}$(app)/${}^{R''}A_0^{(0)}$(app) and ${}^{R''}A_0^{(4)}$(app)/${}^{R''}A_0^{(0)}$(app) parameters listed in Table 1 show a better qualitative correlation with those predicted for the $K'' = 4$ and $K'' = 5$ states where the **J** vector is restricted to lie in the $x'z'$ plane of the body-fixed frame (see Table 2).

B.2. REMPI Spectra: Nascent CD$_3$ Rotational Population Distributions. High-sensitivity, velocity-selected REMPI spectra of the $4p_z 0_0^0$ transition were collected for fixed geometries of the probe laser ($\chi = 0°, 35°, 90°$) after photolysis of DMS-d_6 at $\lambda_{\text{PHOT}} = 215$, 218.5, and 222 nm. Typical REMPI spectra at 218.5 nm are shown in Figure 4a; assignments of the R ($\Delta N = +1$) and S ($\Delta N = +2$) rotational branches can be found in ref 9. Calculated REMPI spectra with intensities computed from eq 9, using a line-width function described elsewhere[6] to account for natural and instrumental line-broadening effects (fwhm ≈ 1.6 cm^{-1}), are shown for comparison with experiment in Figure 4b−d. The nascent population distribution was obtained by empirical weighting of the $n(N'',K'')$ quantum states to achieve the best fit with the experimental spectra. The simulations begin with comparison of the spectra at $\chi = 0°$, because at this geometry, the P_q^k line-strength factors with $q \neq 0$ are zero and, hence, fitting is dependent on only the (**v**, **J**) correlation; consequently, the simulations shown in Figure 4b−d for $\chi = 0°$ are identical. The K'' population distribution within each N'' manifold is modeled empirically following the methodology of Pisano et al.[38] Within that formalism, the K'' population function for each value of N'' is assumed to have the form of a Boltzmann distribution with an effective temperature of $T_{K''}(N'')$. For the oblate methyl fragment, a low, positive $T_{K''}$ value corresponds to a propensity for rotation about the C_3 axis (*high* K'', spinning motion), whereas at the other extreme, a negative $T_{K''}$ value

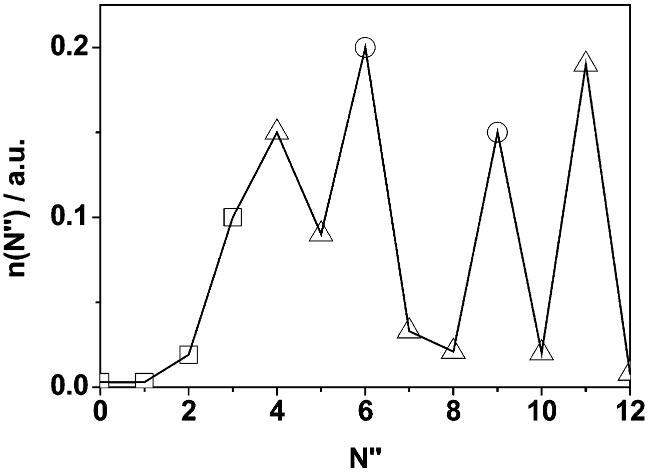

Figure 7. Empirically fitted N'' state populations extracted from simulations of the REMPI spectra of nascent CD_3 fragments following photodissociation at $\lambda_{PHOT} = 218.5$ nm. Circles, squares, and triangles indicate high-K'' (spinning motion), low-K'' (tumbling motion), and intermediate-K'' propensities, respectively.

corresponds to a tendency for rotation about an axis in the plane of the methyl radical (*low* K'', tumbling motion).

As a consequence of the differing K'' dependencies of the $P_q^k(N'',K'',N',K')$ line-strength factors for the R and S branches, $T_{K''}$ for each N'' state could be estimated by comparing the relative intensities of common R and S transitions. Low-N'' states ($N'' = 1-3$) are better described by a low-K'' propensity [e.g., in both spectra, the S(3) transition is stronger than its R(3) counterpart], whereas a high-K'' propensity better describes the higher-N'' states (e.g., for $N'' > 5$ the S branch is barely observed in any of the spectra). An intermediate-K'' propensity was found for the states between these limits ($N'' = 4$ and $N'' = 5$) and for the state $N'' = 11$. The spectrum at $\chi = 90°$ is particularly sensitive to the P_q^k line-strength factors with $q \neq 0$ so that, provided that the $n(N'',K'')$ is reliable, comparison of experiment and simulation at this geometry provides an indication of the full ($\boldsymbol{\mu}$, **v**, **J**) correlation. The simulations in Figure 4b represent the best qualitative agreement with experiment, indicating that the **J** vector lies preferentially in the $x'z'$ frame after dissociation and that the nascent ($\boldsymbol{\mu}$, **v**, **J**) correlation is well described by the axial impulsive model.

The N'' distribution determined from the data at $\lambda_{PHOT} = 218.5$ nm is plotted in Figure 7 and cannot be fitted with a Boltzmann distribution of nascent rotational CD_3 states; this finding is examined in section IV.

The above analysis was repeated for the REMPI spectra obtained following photolysis at the other wavelengths studied. The empirically fitted N'' distributions were found to be almost identical in each case, with an average rotational energy of the nascent $CD_{3(v=0)}$ fragment, $\langle E_{ROT}\rangle \approx 200$ cm^{-1}, representing only ~1% of the total available energy, in reasonable agreement with previous experiments[5-9] at other photolysis wavelengths within the first absorption band.

IV. Discussion

A. Implications of the Experimental Data. The most important experimental results are as follows: (i) DMS dissociates via reaction 1 across the entire first absorption band (215−230 nm). (ii) A large fraction of the available energy is deposited into photofragment translation, $\langle x\rangle \approx 0.7-0.8$, decreasing as a function of excitation energy. (iii) The anisotropy parameter β is negative and converges toward its limiting value for an instantaneous, perpendicular-type transition ($\beta = -1$) at the onset of the first absorption band (~230 nm). (iv) Only about 5% of the available energy is channeled into internal excitation of the methyl fragment, the rotational excitation of which is found to be nonstatistical. (v) ($\boldsymbol{\mu}$, **v**, **J**) correlations are shown to be well approximated by an axial impulsive model, with a noncylindrically symmetric distribution of the **J** vector with respect to **v**.

In general, these observations corroborate earlier evidence that photodissociation of DMS in the first absorption band occurs via an abrupt, impulsive mechanism following a perpendicular polarized transition. However, points ii and iii would seem to imply that dissociation does not occur by direct coupling to a repulsive surface, where one would generally expect the anisotropy and fraction of available energy in translation to be invariant with respect to excitation energy. In the following section, each of the above findings is rationalized with a view toward understanding the dissociation mechanism that is responsible. It is shown that the set of results presented here is consistent with the earlier picture developed for the photodissociation of the lighter sulfur homologue H_2S molecule,[44] where photoabsorption to a bright bound state of $^1B_1$ symmetry is strongly predissociated by a repulsive dark state of $^1A_2$ symmetry.

B. Energy Partitioning. Knowledge of the way in which the available energy, E_{av}, is partitioned into the photofragment degrees of freedom can provide information on both the energetics and dynamics of the reaction. Simple models predicting this energy partitioning following molecular photodissociation can be divided into two categories. *Statistical models* are most appropriate for slow reactions occurring on barrierless potential energy surfaces; all product states are equally likely within a series of constraints. Examples include prior distributions[45] in which energy and linear momentum are conserved, and phase space theory[46] (PST), which also conserves angular momentum. *Impulsive models*[47] are more suitable for direct dissociation on a repulsive potential.

The energy available, E_{av}, to be partitioned between the degrees of freedom of the photofragments CD_3 and SCD_3 is given by the following expression

$$E_{av} = E_{photon} - D_0(CD_3S{-}CD_3) + E_{int} \qquad (14)$$

where E_{photon} is the photolysis photon energy, $D_0(CD_3S{-}CD_3)$ is the zero-point bond dissociation energy (313.59 kJ mol^{-1} from ref 17), and E_{int} is the internal energy of the parent molecule. Most of the contributions to E_{int} should involve the low-frequency modes, skeletal bends, and methyl torsions that are expected to undergo partial or complete relaxation in the supersonic expansion.

Although weak excitation of the "umbrella" vibrational mode of the nascent CD_3 fragments to that reported in a previous communication from our group[5] (<4% of the available energy) was also observed in this work at all photolysis wavelengths, for the purpose of comparison with theoretical predictions, it is assumed that vibrational excitation of the methyl fragment is negligible at all photolysis wavelengths. The resulting experimental values for $\langle x\rangle$ can then be directly compared with average translational release fractions, $\langle f_T\rangle$, calculated by theory. The average fractions $\langle x\rangle$ obtained from the experimental measurements are listed in Table 4 for each photolysis wavelength studied.

The large fraction of available energy found in product translation clearly indicates that statistical theories are inappropriate for describing the dissociation dynamics of this system.

TABLE 4: Experimentally Determined Anisotropy Parameters, β, and Average Fractions of Available Energy Deposited into Photofragment Translation, $\langle x \rangle$, as Functions of the Photolysis Laser Wavelength, λ_{PHOT}[a]

	observed		impulsive		
λ_{PHOT} (nm)	$\beta \pm 0.1$	$\langle x \rangle \pm 0.02$	BW $\langle f_T \rangle$	V-AID $\langle f_T \rangle$	hybrid $\langle f_T \rangle$
229[c]	−0.9	0.80	0.66	0.87	0.83
222	−0.8	0.77	0.66	0.87	0.77
218.5	−0.8	0.75	0.66	0.87	0.75
215	−0.8	0.72	0.66	0.87	0.73

[a] Experimental values are compared with calculations of $\langle f_T \rangle$ based on the Bush and Wilson (BW) impulsive (ref 47), V-AID impulsive (ref 51), and hybrid models for energy partitioning. [c] Ref 6.

The impulsive model is based on the assumption that the available energy acts as a repulsive potential along the breaking bond, with the conservation of linear and angular momentum determining the energy partitioning among fragments. A limiting impulsive formalism for energy partitioning between photofragment degrees of freedom was devised by Busch and Wilson[47] (BW) for the modeling of triatomic molecular photodissociation. The basic idea of this model, based on the spectator stripping model used for nuclear[48] and bimolecular[49] reactions, is that the atoms of the dissociating bond recoil so sharply that the energy is released before the other atom has had time to respond. The model has been used frequently since and has undergone several refinements, including the extension to polyatom−polyatom half-collisions.[50] A modification of the impulsive model was proposed by the same authors[47] where product vibrational degrees of freedom were decoupled from the dissociation coordinate. Later, Lim[51] noted that this modified impulsive model does not conserve linear momentum and implemented a new vibrationally adiabatic impulsive dissociation model (V-AID), in which the method of undetermined Lagrange multipliers was used to decouple vibrations from the dissociation reaction coordinate.

Calculations using the BW and V-AID impulsive models, where it is assumed that the geometry of the excited parent molecule is that of the ground state calculated by Manaa and Yarkony,[4] are compared with the experimental data in Table 4. This is a reasonable approximation, given that the dominant excitation is nonbonding ($3b_1$) to Rydberg ($9a_1$) and, consequently, would not be expected to provoke a dramatic change in equilibrium geometry. The preferential partitioning of available energy into translational recoil is qualitatively reproduced by the BW model; however, this model predicts substantial vibrational excitation of the v_2 umbrella mode of the CD_3 fragment (∼24% of the available energy). In contrast, only weak excitation (<4% of the available energy) of this mode has been observed experimentally.[5] As a consequence, the BW $\langle f_T \rangle$ fractions are smaller than the experimental values. Accounting for this observation, it is suggested that the dissociation of DMS mimics the photolysis of ICH_3 in its first absorption band,[52−56] where the CH_3 moiety gradually relaxes to its equilibrium planar geometry prior to cleavage of the C−S bond. The surplus energy not observed as CD_3 vibrational excitation must be partitioned into the other available degrees of freedom of the fragments. Comparison of the experimental data with the V-AID model, where vibrational energy in the methyl fragment is assumed to be frozen at its zero-point energy, predicts the translational energy release to within 10% of the observed value at 229 nm, supporting the suggestion that the photodissociation occurs along a path in which the potential energy in the CD_3 bending coordinate is a minimum for a given CS−C distance.

The observed decreasing fraction of available energy deposited into translation with increasing excitation energy (see Table 4), also reported in a recent ion imaging study of the undeuterated molecule in the first absorption band,[8] suggests that an exit barrier on the excited potential energy surface mediates the dissociation dynamics. This would certainly be consistent with the work of Manaa and Yarkony,[4] where a surface of conical intersections caused by the avoided crossing of the excited $1^1A''$ and $2^1A''$ surfaces (an *accidental same-symmetry* conical intersection in the classification of Yarkony[57]) was located in the Franck−Condon region of the $\tilde{X}^1A_1$ state. Figure 8a depicts the excited $1^1B_1(1^1A'')$ and $1^1A_2(2^1A'')$ surfaces of Manaa and Yarkony,[4] calculated as a function of the CS−C dissociation coordinate with all other geometrical parameters fixed to the ground-state equilibrium structure. A qualitative explanation of the experimental results can be obtained by considering the following points: After one-photon absorption, a superposition of states on both the $1^1B_1(1^1A'')$ and $1^1A_2(2^1A'')$ potential energy surfaces is produced, the latter as a result of vibronic coupling of the 1^1B_1 and 1^1A_2 states through the CSC asymmetric stretching mode. In the case of the dominant, symmetry-allowed excitation to the 1^1B_1 state, dissociation proceeds mainly as a consequence of zero-point nonsymmetric vibrational motion, through nonadiabatic coupling to the repulsive 1^1A_2 surface over a barrier in the dissociation coordinate formed by the avoided crossing. In the case of the vibronically allowed absorption to the $1^1A_2(2^1A'')$ state, excitation at wavelengths corresponding to the region of conical intersections, at the base of the excited potential in Figure 8a, facilitates almost instantaneous dissociation. However, at shorter λ_{PHOT}, molecules are produced with higher, Franck−Condon-favored, asymmetric stretching vibrational excitation. These excited molecules must undergo, at least partially, intramolecular vibrational redistribution (IVR) to reach a surface of conical intersections at their corresponding energy. These processes are depicted schematically in Figure 8b and c using the torsional degree of freedom as an example energy redistributing vibrational mode through which the evolving excited system could be funneled toward a seam of conical intersections. IVR processes are particularly facile in polyatomic molecules, where low-frequency torsional and/or bending modes can dramatically increase rovibrational state densities.

Because energy partitioning in the purely impulsive type models is based solely on mass factors, such models predict that the fraction of available energy in translation is invariant with respect to the excitation energy. However, the nature of the dissociation mechanism implied by the above discussion requires a model that reflects both the impulsive nature of the half-reaction at the conical intersection and the statistical redistribution occurring at higher energies. For the excited-state dissociation of a polyatomic molecule with as many degrees of freedom as DMS, accurate quantum dynamical calculations are not yet feasible. Nevertheless, qualitatively useful impulsive−statistical treatments have been proposed by Sonobe et al.,[58] Gejo et al.,[59] North et al.,[60] and Osborn et al.[61] The common theme of these models is the partitioning of the available energy, E_{av}, for the products into two independent reservoirs: E_{stat}, the available energy in excess of the barrier, and E_{imp}, the height of the barrier with respect to the products (see Figure 8a). The treatment of each energy reservoir is dependent on the respective theories, although the qualitative predictions are not expected to change significantly. Here, we assume that the V-AID model[51] accurately represents the impulsive "vibrationally adiabatic" part of the dissociation mentioned above, while the partitioning of

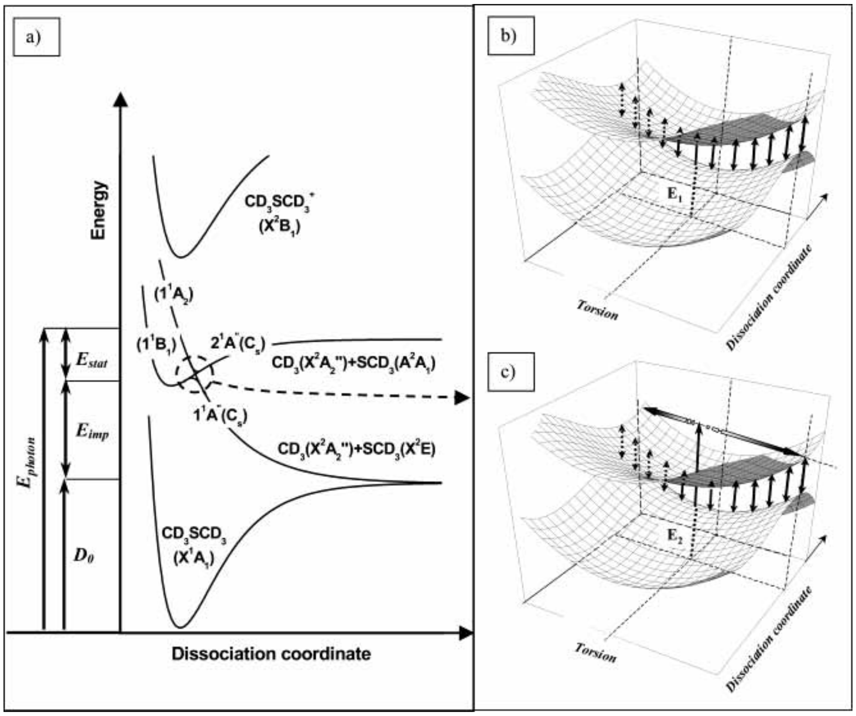

Figure 8. (a) Schematic diagram illustrating the electronic states involved in the photodissociation of DMS at 215−229 nm with the various energy quantities (E_{imp} and E_{stat}) used in the hybrid statistical−impulsive model described in the text. (b) Schematic representation of a 2D cut of the $1^1B_1(1^1A'')$ and $1^1A_2(2^1A'')$ excited potential energy surfaces as a function of the torsional and CS−C reaction coordinates. The vertical double arrows indicate a seam of conical intersections. Excitation (E_1) of low asymmetric stretching vibrational levels on the $1^1A_2(2^1A'')$ surface facilitates almost instantaneous dissociation by direct access of the conical intersection. (c) Excitation (E_2) of higher asymmetric stretching levels on the $1^1A_2(2^1A'')$ surface can reach a seam of conical intersections by IVR among other vibrational modes. The torsional mode was chosen as an illustrative case

TABLE 5: Ground-State DMS-d_6 Vibrational Energies Calculated at the B3LYP/6-31G(d,p) Level of Theory Using Gaussian98

mode	energy (cm^{-1})	product assignment[a]
CD_3 asym. torsion υ_1	128.9	rotation
CD_3 sym. torsion υ_2	130.5	
C−S−C deformation υ_3	221.5	
C−S−C sym. stretch υ_4	623.8	translation
C−S−C asym. stretch υ_5	689.4	
in-plane CD_3 asym. rock υ_6	684.3	rotation
out-of-plane CD_3 asym. rock υ_7	710.3	
out-of-plane CD_3 sym. rock υ_8	751.2	
in-plane CD_3 sym. rock υ_9	837.2	
CD_3 asym. deformation υ_{10}	1024.2	vibration
CD_3 sym. deformation υ_{11}	1042.3	
out-of-plane asym. deformation υ_{12}	1061.4	
out-of-plane sym. deformation υ_{13}	1068.5	
out-of-plane asym. deformation υ_{14}	1074.9	
out-of-plane sym. deformation υ_{15}	1078.1	
in-plane sym. C−H stretch υ_{16}	2174.7	
in-plane asym. C−H stretch υ_{17}	2176.9	
out-of-plane sym. stretch υ_{18}	2305.7	
out-of-plane asym. stretch υ_{19}	2311.5	
out-of-plane asym. stretch υ_{20}	2319.4	
out-of-plane sym. stretch υ_{21}	2320.5	

[a] Product degree of freedom assignments used in the partitioning of the statistical reservoir, E_{stat}, (see text) are indicated.

the statistical fraction follows the recipe of North et al.[60] where energy is assumed to be freely distributed among the parent vibrational modes. Distribution of the statistical energy among photofragment degrees of freedom is achieved by the judicious assignment of three ensembles of vibrational parent modes correlating with translational, rotational, or vibrational motion of the products.[60] For the calculation of the statistical reservoir in this work, ground-state DMS vibrational frequencies calculated at the B3LYP/6-31G(d,p) level of theory with the Gaussian98 software[62] were used as an approximation to those of the excited state; these are listed in Table 5, together with their respective product mode assignments. The Whitten−Rabinovitch method[63] was used to calculate the vibrational density of states for all ensembles. Because the calculations of Manaa and Yarkony[4] indicate that the surface of conical intersections occurs in the Franck−Condon region accessed from the ground $\tilde{X}^1A_1$ state, the first feature in the absorption spectrum (∼234 nm) of ref 8 is taken as a lower limiting value for the excitation energy corresponding to the impulsive barrier. E_{imp} therefore takes the value $E_{\text{photon}} - D_0 = 16\,538$ cm^{-1} above the ground-state products, while the statistical reservoir is $E_{\text{stat}} = E_{\text{photon}} - E_{\text{imp}}$. The predictions from this *hybrid* model are listed in Table 4 for comparison with the experimental data. Although the excellent agreement between the values might be fortuitous, it does suggest that the above model provides a qualitatively correct description of the dissociation mechanism taking place.

C. Anisotropy and Vector Correlations of the Photoproducts. *C.1. Recoil Anisotropy β.* The anisotropy parameter β is sensitive to both the lifetime, τ, and the geometry of the dissociating molecule. For an instantaneous dissociation, β is related to the dissociation geometry by

$$\beta = 2\langle P_2(\cos \theta_t')\rangle \tag{15}$$

where θ_t' is the angle between the absorbing transition dipole moment $\boldsymbol{\mu}$ and the recoil velocity of the photofragment $\mathbf{v}$. The anisotropy parameter therefore ranges from $\beta = -1$, for a dissociation where $\mathbf{v}$ is perpendicular to $\boldsymbol{\mu}$, to $\beta = 2$, where the two vectors are parallel. Because the transition moment for the

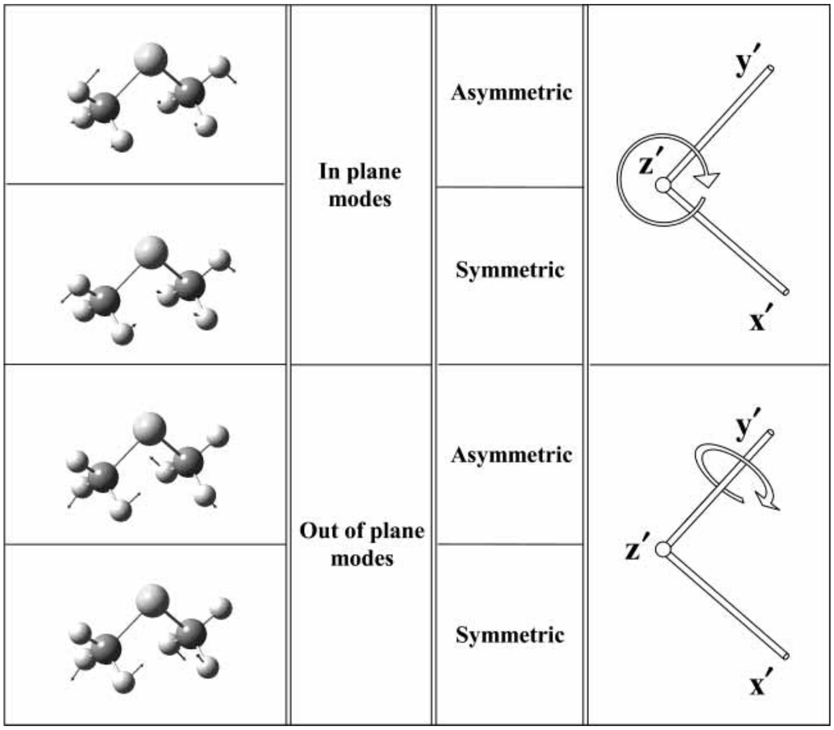

Figure 9. Rocking methyl parent vibrational modes can induce rotational angular momentum of the photofragment with **J** perpendicular to **v**(x'). The two in-plane modes (upper) exert a torque about the z' axis of the molecule-fixed frame (**J** in plane $x'z'$), whereas the two out-of-plane rocking modes (lower) result in angular momentum about the y' axis (**J** in plane $x'y'$).

$1^1B_1 \leftarrow \tilde{X}^1A_1$ transition is directed perpendicular to the plane containing the C−S−C framework, the axial recoil limiting anisotropy parameter for excitation in the first absorption band is $\beta = -1$. As shown in Table 4, the measured recoil anisotropy parameter β is close to this limit at all of the photolysis wavelengths studied, although this observation should be treated with care given that, for a jet-cooled sample of a polyatomic molecule, the rotational period is long and so, therefore, is the time scale required for significant loss of anisotropy. Assuming that parent rotation is the dominant factor in the "washing out" of the limiting anisotropy, then an approximation for the excited-state lifetime, τ, can be obtained from the classical expression for the reduced effective anisotropy parameter used for the treatment of diatomic molecules[64]

$$\beta_{\text{eff}} = \beta\left(\frac{1 + \omega^2\tau^2}{1 + 4\omega^2\tau^2}\right) \tag{16}$$

where ω is the angular velocity of the parent rotation. Calculating the average rotational period of the excited state assuming a rigid ground-state geometry[4] predicts upper limiting excited-state lifetimes of ∼1.3 and ∼1.9 ps for the experimentally measured anisotropy parameters $\beta_{\text{eff}} = -0.9$ (at $\lambda_{\text{PHOT}} = 229$ nm) and $\beta_{\text{eff}} = -0.8$ (at $\lambda_{\text{PHOT}} = 222$, 218.5, and 215 nm), respectively. These values would certainly seem reasonable, bearing in mind the suggestion that at least partial IVR occurs before bond rupture and given that the benchmark for relaxation in molecules that are about the same size as DMS is ∼1 ps.[63]

C.2. (μ, v, J) Correlations. Although far from providing a comprehensive analysis, forward simulations of the polarization-dependent REMPI spectra provide strong evidence that the proposed axial impulsive model adequately describes the dissociation mechanism. As was suggested to be the case in a previous study,[9] the analysis here indicates that the **J** vector does not have cylindrical symmetry about **v**.

Figure 9 shows a schematic diagram of the dissociating parent DMS molecule. Strictly speaking, because the model impulse passes through the center of mass of the methyl fragment, only vibrational motion of the excited parent molecule can induce its rotational excitation. As shown in the figure, the two in-plane rocking modes (υ_6 and υ_9) exert a torque about the z' axis of the molecule-fixed frame (**J** in plane $x'z'$), whereas the two out-of-plane rocking modes (υ_7 and υ_8) result in angular momentum about the y' axis (**J** in plane $x'y'$). Hence, a cylindrically symmetric distribution of **J** about **v** should be expected, unless a further source of in-plane torque can be invoked to explain the experimental observation that **J** is preferentially located in plane $x'z'$. In the hybrid model calculations mentioned above, the υ_3 C−S−C deformation mode was included in the rotational product ensemble, following the guidelines of North et.al.,[60] although much of that angular momentum is expected to be converted into orbital motion of the products. It is tentatively suggested here that this mode could be the source of the additional in-plane torque, as well as the distortion of the CSC bond angle (105.5° at the equilibrium geometry compared to 112° on the surface of conical intersections) that is expected to occur on reaching the surface of conical intersections.[4]

D. Rotational Excitation of the Methyl Fragment. As noted on above, parent vibrational motion is the main source of the angular momentum imparted to the methyl fragments, giving rise to the rotational state N population distribution shown in Figure 7. The two torsional (υ_1 and υ_2) and four CD_3 rocking (υ_6−υ_9) modes are most strongly correlated with methyl fragment rotational excitation. Particularly, in a Franck−Condon-type picture, the torsional modes are expected to be well correlated with "spinning", high-K''-state propensity methyl fragments, because the parent vibrational wave function is very similar to that of the product free rotor. Reference to Table 5 shows that the two torsional modes vibrational frequencies are

TABLE 6: Average Energies of the $N'' = 6$ and $N'' = 9$ States Compared with the First Three Parent Torsional Energy Levels

torsion (v_1, v_2)	torsion energy (cm^{-1})	N''	average energy (cm^{-1})
(0, 0)	131.8	6	126.2
(1, 0), (0, 1)	258.6, 260.2	9	256.2

almost the same; the zero-point ($v_1 = 0$, $v_2 = 0$) combination has an energy of ~130 cm^{-1}. This energy is not quite sufficient to account for the average excitation observed (~200 cm^{-1}), although a significant contribution to product angular momentum should also be expected from the CD$_3$ rocking modes (v_6-v_9). Previous investigations[54,56,65,66] on the dissociation of cold ICD$_3$ following absorption to the A band ($\lambda_{\mathrm{PHOT}} \approx 266$ nm) reported "tumbling", low-K''-state-propensity, nascent methyl fragments. It was concluded that approximately half of the rotational energy observed (~94 cm^{-1}) originates from zero-point I−C−D$_3$ bending vibrational energy and approximately half from a torque exerted by the bent superposition of excited states. Assuming that a similar quantity of energy is channeled from the DMS "rocking" modes, then this would approximately make up the balance that is observed experimentally.

Continuing the comparison with ICD$_3$ photodissociation, the N'' states in the present work ($N'' = 3-12$) that favor a higher-K'' propensity mirror more closely the study of the A band photodissociation of warm ICD$_3$ reported by Black et al.[67] Presumably, in that case, the warm, spinning motion of the prolate ICD$_3$ parent preferentially correlates with the high-K'' propensity of the methyl photofragment. In contrast, the rotational motion of the cold, tumbling ICD$_3$ can only correlate with orbital angular momentum of the fragments. Rotational excitation of the methyl fragment must then originate from ICD$_3$ zero-point vibrational motion that can only correlate with a nascent low-K'' propensity given that there are no parent torsional modes.

The above considerations allow some tentative comments to be made on the N'' population distribution extracted from the REMPI spectra (see Figure 7). In the limit of very similar wave functions for the parent vibration and methyl free rotor degrees of freedom, N'' rotational states in close resonance with the torsional energies are expected to be preferentially populated. Shown in Table 6 is a comparison of the average energies of the prominent $N'' = 6$ and $N'' = 9$ states, both found to have high-K''-state propensity, as evidenced by the nonappearance of their corresponding S transitions, with the first three torsional energy levels of the parent molecule. The energies are sufficiently close to be speculatively assigned as resonantly associated with the torsional modes, bearing in mind the approximate nature of the $T_{K''}$ temperature and the ground-state approximation to the torsional frequencies of the dissociating DMS parent. As one might expect for a cold sample, the $N'' = 6$ state corresponding to the (0, 0) zero-point torsional vibration is preferentially populated, though some population of the (1, 0) and (0, 1) levels should also occur, as a consequence of both nonvertical transitions and also the retention of the initial Boltzmann population of the ground state. Weak excitation of these higher levels could account for the apparent tendency for formation of the $N''= 9$ state.

Because the states $N'' = 0-3$ appear to be formed with a low-K'' propensity, it would seem reasonable to assign their origin to the rocking vibrational motion (v_6-v_9) of the parent DMS. The remaining N'' states are presumably populated by a less specific continuum of dissociation mechanisms involving parent vibrational and rotation, as well as energy-redistribution processes considered previously. The correlation of parent vibrational motion with fragment rotation is less clear for the prominent peak obtained at $N''= 11$. As remarked in section III.B.2, this N'' state is associated with an intermediate K'' propensity and might be tentatively assigned to mixed contributions from rocking and torsional modes of the parent molecule.

V. Conclusions

This paper describes the results of a further investigation of the photofragmentation dynamics of DMS following excitation at a variety of wavelengths within the first absorption band. In accordance with previous work,[5−9] measurements of REMPI-TOF profiles of the nascent CD$_3$ products indicate a strongly anisotropic dissociation, with approximately 70−80% of the available energy appearing as relative fragment translation. At all of the photolysis energies studied, only weak vibrational excitation of the umbrella mode of the methyl fragment is observed, which is contrary to intuitive expectations for an axial repulsion along the CS−C bond. This finding is rationalized in terms of a vibrationally adiabatic dissociation that mirrors that following the excitation of ICD$_3$ to its first absorption band, where the CD$_3$ moiety gradually relaxes to its equilibrium planar geometry prior to cleavage of the CS−C bond. Analysis of the REMPI spectra reveals similar weak excitation in the rotational degree of freedom of the methyl fragment, corresponding to approximately 1% of the available energy. Thus, the available energy is partitioned primarily into translational recoil and internal excitation, presumably mainly rotational, of the SCD$_3$ fragment.

At $\lambda_{\mathrm{PHOT}} = 229$ nm, the observed translational energy released into the products is very similar to that predicted by a modified impulsive model that takes into account the vibrational adiabaticity of the CD$_3$ fragment. At higher excitation energies, the fraction of available energy deposited into product translation decreases, a finding that cannot be rationalized in terms of either the modified impulsive model or a statistical model in which too little translational excitation is predicted. A possible interpretation of the qualitative features of the excited-state surface, aided by previous theoretical calculations,[4] suggests that a more realistic picture should combine at least partial statistical redistribution prior to an impulsive release of energy. A hybrid statistical−impulsive dissociation model predicts a photolysis wavelength dependence of the translational energy release that compares favorably with experimental measurements.

Rotational excitation of the methyl fragments is thought to arise mainly from zero-point vibrational motion of the dissociating parent. Low-N'' states ($N''= 0-3$) are produced with a low-K'' propensity, indicating that they originate from rocking vibrational motion. In contrast, higher-N'' states are formed with a high-K'' propensity, correlating with torsional parent modes. Preferentially populated N'' states are tentatively suggested to be resonantly associated with torsional vibrational frequencies of the dissociating DMS parent. A simple model used to approximate the correlations of the $\boldsymbol{\mu}$, $\mathbf{v}$, and $\mathbf{J}$ vectors just after dissociation satisfactorily reproduces the observed probe-polarization-dependent, velocity-selected REMPI spectra.

Acknowledgment. We dedicate this article to the memory of the late Professor Richard Bersohn, whose scientific achievements along the years have inspired and encouraged research in the field of photodissociation of molecules. I.T. thanks the Spanish Ministry of Science and Technology (MCYT) for financial support within the program "Ramon y Cajal". J.B. acknowledges financial support from the EU Research Training

Network “Reaction Dynamics” HPRN-CT-1999-00007. This project was financed by the Spanish MCYT under Project BQU2002-04627-C02-02. The facilities provided by the “CAI de Espectroscopía Multifotónica de la Universidad Complutense de Madrid” are gratefully aknowledged.

References and Notes

(1) Busch, G. E.; Wilson, K. R. *J. Chem. Phys.* **1972**, *56*, 3638.

(2) Dzvonik, M.; Yang, S.; Bershon, R. *J. Chem. Phys.* **1974**, *61*, 4408.

(3) Bersohn, R. *J. Phys. Chem.* **1984**, *88*, 5145.

(4) Manaa, M. R.; Yarkony, D. R. *J. Am. Chem. Soc.* **1994**, *116*, 11444.

(5) Martínez-Haya, B.; Zapter, I.; Quintana, P.; Menéndez, M.; Verdasco, E.; Santamaría, J.; Bañares, L.; Aoiz, F. J. *Chem. Phys. Lett.* **1999**, *311*, 159.

(6) Martínez-Haya, B.; Aoiz, F. J.; Bañares, L.; Quintana, P.; Verdasco, E. *J. Phys. Chem. A* **2000**, *104*, 10150.

(7) Quintana, P.; Delmdahl, R. F.; Parker, D. H.; Martínez-Haya, B.; Aoiz, F. J.; Bañares, L.; Verdasco, E. *Chem. Phys. Lett.* **2000**, *325*, 146.

(8) Martínez-Haya, B.; Quintana, P.; Bañares, L.; Samartzis, P.; Smith, D. J.; Kitsopoulos, T. N. *J. Chem. Phys.* **2001**, *114*, 4450.

(9) Barr, J.; Torres, I.; Bañares, L.; Verdasco J. E.; Aoiz, F. J. *Chem. Phys. Lett.* **2003**, *373*, 550.

(10) Touke, I.; Hiraya, A.; Shobatake, K. *Chem. Phys.* **1989**, *130*, 401.

(11) Morgan, R. A.; O-Ewing, A. J.; Ashfold, M. N. R.; Buma, W. J.; Wales, N. P. L.; de Lange, C. A. *J. Chem. Soc., Faraday Trans.* **1995**, *91*, 3339.

(12) Scott, J. D.; Causley, G. C.; Russell, B. R.; *J. Chem. Phys.* **1973**, *59*, 6577.

(13) Mason, W. R. *J. Phys. Chem.* **1996**, *100*, 8139.

(14) Rao, P. M.; Copeck, J. A.; Knight, A. R. *Can. J. Chem.* **1967**, *45*, 1369.

(15) Callear, A. B.; Dickinson, D. R. *Trans. Faraday. Soc.* **1970**, *67*, 1987.

(16) Rao, P. M.; Knight, A. R. *Can. J. Chem.* **1972**, *50*, 844.

(17) Nourbakhsh, S.; Norwood, K.; Yin, H. M.; Liao, C. L.; Ng, C. Y. *J. Chem. Phys.* **1991**, *95*, 5014.

(18) Lee, Y. R.; Chiu, C. L.; Lin, S. M. *J. Chem. Phys.* **1994**, *100*, 7376.

(19) Ogorzalek Loo, R.; Hall, G. E.; Haerri, H. P.; Houston, P. L. *J. Phys. Chem.* **1988**, *92*, 5.

(20) Aoiz, F. J.; Díez-Rojo, T.; Herrero, V. J.; Martínez-Haya, B.; Menéndez, M.; Quintana, P.; Ramonat, L.; Tanarro, I.; Verdasco, E. *J. Phys. Chem.* A **1999**, *103*, 823.

(21) Black, J. F.; Powis, I. *J. Chem. Phys.* **1988**, *89*, 3986.

(22) Wiley: W. C.; McLaren, I. H. *Rev. Sci. Instrum.* **1955**, *26*, 1150.

(23) Simpson, W. R.; Orr-Ewing, A. J.; Rakitzis, T. P.; Kandel, S. A.; Zare, R. N. *J. Chem. Phys.* **1995**, *103*, 7299.

(24) Mons, M.; Dimicoli, I. *J. Chem. Phys.* **1989**, *90*, 4037.

(25) Cheng, P. Y.; Zhong, D.; Zewail, A. H. *J. Chem. Phys.* **1996**, *105*, 6216.

(26) Bergmann, K.; Carter, R. T.; Hall, G. E.; Huber, J. R. *J. Chem. Phys.* **1998**, *109*, 474.

(27) McGivern, S. W.; Li, R.; Zou, P.; North, S. W. *J. Chem. Phys.* **1999**, *111*, 5771.

(28) Zare, R. N. *Mol. Photochem.* **1972**, *4*, 1.

(29) Vasudev, R.; Zare, R. N.; Dixon, R. N. *J. Chem. Phys.* **1984**, *80*, 4863.

(30) *Simion-3D*, version 6.0; Idaho National Engineering Laboratory, EG&G Idaho Inc.: Idaho Falls, ID, 1987.

(31) Dubs, M.; Brühlmann, U.; Huber, J. R. *J. Chem. Phys.* **1986**, *84*, 3106.

(32) Mo, Y.; Katayanagi, H.; Heaven, M. C.; Suzuki, T. *Phys. Rev. Lett.* **1996**, *77*, 830.

(33) Nestorov, V. K.; Hinchliffe, R. D.; Uberna, R.; Cline, J. I.; Lorenz, K. T.; Chandler, D. W. *J. Chem. Phys.* **2001**, *115*, 7881.

(34) Bass, M.; Brouard, M.; Clark, A.; Vallance, C. *J. Chem. Phys.* **2002**, *117*, 8723.

(35) Dixon, R. N. *J. Chem. Phys.* **1986**, *85*, 1866.

(36) Uberna, R.; Hinchliffe, R. D.; Cline, J. I. *J. Chem. Phys.* **1995**, *103*, 7934.

(37) Zare, R. N. *Angular Momentum*; Wiley-Interscience. New York, 1988.

(38) Pisano, P. J.; Cline, J. I. *J. Chem. Phys.* **2000**, *112*, 6190.

(39) Allkins, J. R.; Hendra, P. J. *Spectrochim. Acta* **1966**, *22*, 2075.

(40) Kummel, A. C.; Sitz, G. O.; Zare, R. N. *J. Chem. Phys.* **1986**, *85*, 6874.

(41) Rakitzis, T. P.; Hall, G. E.; Costen, M. L.; Zare, R. N. *J. Chem. Phys.* **1999**, *111*, 8751.

(42) Kummel, A. C.; Sitz, G. O.; Zare, R. N. *J. Chem. Phys.* **1988**, *88*, 6707.

(43) Kummel, A. C.; Sitz, G. O.; Zare, R. N. *J. Chem. Phys.* **1988**, *88*, 7357.

(44) Ashfold, M. N. R.; Mordaunt, D. H.; Wilson, S. H. S. *Adv. Photochem.* **1996**, *21*, 217.

(45) Levine, R. D.; Bernstein, R. B. *Acc. Chem. Res.* **1974**, *7*, 393.

(46) Pechukas, P.; Light, J. C. *J. Chem. Phys.* **1965**, *42*, 3281.

(47) Busch, G. E.; Wilson, K. R. *J. Chem. Phys.* **1972**, *56*, 3625.

(48) Banerjee, M. K. In *Nuclear Spectroscopy*; Academic Press: New York, 1960.

(49) Henglein, A. In *Molecular Beams and Reaction Kinetics*; Academic Press: New York, 1970.

(50) Trentelman, K. A.; Kable, S. H.; Moss, D. B.; Houston, P. L. *J. Chem. Phys.* **1989**, *91*, 7498.

(51) Lim, K. F. *Com. Phys. Commun.* **1996**, *97*, 345.

(52) Shapiro, M.; Bersohn, R. *J. Chem. Phys.* **1980**, *73*, 3810.

(53) Suzuki, T.; Kanamori, H.; Hirota, E. *J. Chem. Phys.* **1991**, *94*, 6607.

(54) Loo, R. O.; Haerri, H. P.; Hall, G. E.; Houston, P. L. *J. Chem. Phys.* **1989**, *90*, 4222.

(55) Zahedi, M.; Harrison, J. A.; Nibler, J. W. *J. Chem. Phys.* **1994**, *100*, 4043.

(56) Eppink, A. T. J. B.; Parker, D. H. *J. Chem. Phys.* **1999**, *110*, 832.

(57) Yarkony, D. R. *Acc. Chem. Res.* **1998**, *31*, 511.

(58) Sonobe, B. L.; Fletcher, T. R.; Rosenfield, R. N. *J. Am. Chem. Soc.* **1984**, *106*, 4352.

(59) Gejo, T.; Takayanagi, M.; Kono, T.; Hanazaki, I. *Chem. Phys. Lett.* **1994**, *218*, 343.

(60) North, S. W.; Blank, D. A.; Gezelter, J. D.; Longfellow, C. A.; Lee, Y. T. *J. Chem. Phys.* **1995**, *102*, 4447.

(61) Osborn, D. L.; Choi, H.; Mordaunt, D. H.; Bise, R. T.; Neumark, D. M.; Rohlfing, C. M. *J. Chem. Phys.* **1997**, *106*, 3049.

(62) Frisch, M. J.; Trucks, G. W.; Schlegel, H. B.; Scuseria, G. E.; Robb, M. A.; Cheeseman, J. R.; Zakrzewski, V. G.; Montgomery, J. A., Jr.; Stratmann, R. E.; Burant, J. C.; Dapprich, S.; Millam, J. M.; Daniels, A. D.; Kudin, K. N.; Strain, M. C.; Farkas, O.; Tomasi, J.; Barone, V.; Cossi, M.; Cammi, R.; Mennucci, B.; Pomelli, C.; Adamo, C.; Clifford, S.; Ochterski, J.; Petersson, G. A.; Ayala, P. Y.; Cui, Q.; Morokuma, K.; Malick, D. K.; Rabuck, A. D.; Raghavachari, K.; Foresman, J. B.; Cioslowski, J.; Ortiz, J. V.; Stefanov, B. B.; Liu, G.; Liashenko, A.; Piskorz, P.; Komaromi, I.; Gomperts, R.; Martin, R. L.; Fox, D. J.; Keith, T.; Al-Laham, M. A.; Peng, C. Y.; Nanayakkara, A.; González, C.; Challacombe, M.; Gill, P. M. W.; Johnson, B.; Chen, W.; Wong, M. W.; Andres, J. L.; Head-Gordon, M.; Replogle, E. S.; Pople, J. A. *Gaussian 98*, revision A.11.4; Gaussian, Inc.: Pittsburgh, PA, 2002.

(63) Robinson, P. J.; Holbrook, K. A. *Unimolecular Reactions*; Wiley-Interscience: New York, 1972.

(64) Jonah, C. *J. Chem. Phys.* **1971**, *55*, 1915.

(65) Chandler, D. W.; Janssen, M. H. M.; Stolte, S.; Strickland, R. N.; Thoman, J. W.; Parker, D. H. *J. Phys. Chem.* **1990**, *94*, 4839.

(66) Janssen, M. H. M.; Parker, D. H.; Sitz, G. O.; Stolte, S.; Chandler, D. W. *J. Phys. Chem.* **1991**, *95*, 8007.

(67) Black, J. F.; Powis, I. *J. Phys. Chem.* **1989**, *93*, 2461.